Rare Metal Materials and Engineering
Volume 54, Issue 9, September 2025
Available online at www.rmme.ac.cn

Science Press

Cite this article as: Wu Daogao, Zhang Lu, Xu Minglei, et al. Effects of Sc Content on Microstructure and Thermophysical Properties of Al-*x*Sc Alloys[J]. Rare Metal Materials and Engineering, 2025, 54(09): 2220-2231. DOI: https://doi.org/10.12442/j.issn.1002-185X.20240809.

ARTICLE

Effects of Sc Content on Microstructure and Thermophysical Properties of Al-*x*Sc Alloys

Wu Daogao[1,2], Zhang Lu[1], Xu Minglei[1,2], Feng Jing[3], Li Shuan[1,2], Zhang Xiaowei[1,2], Wang Zhiqiang[1,2], Yang Hongbo[1,2], Dong Ruifeng[1,2], Chen Xihao[4], Wang Ning[5]

[1] GRIREM Advanced Materials Co., Ltd, Beijing 100088, China; [2] GRIREM HI-TECH Co., Ltd, Langfang 065201, China; [3] Guobiao (Beijing) Testing & Certification Co., Ltd, Beijing 100088, China; [4] School of Materials Science and Engineering, Chongqing University of Arts and Sciences, Chongqing 402160, China; [5] Key Laboratory of High Performance Scientific Computation, School of Science, Xihua University, Chengdu 610039, China

Abstract: AlScN piezoelectric films prepared by AlSc alloy sputter targets are essential materials for 5G radio frequency filters. The thermophysical properties of AlSc alloy targets are closely related to their welding processes and applications. Al-*x*Sc alloys (*x*=5, 10, 15, 20, 25, at%) were prepared by vacuum induction melting, whose purity is mainly determined by the raw materials and the production process. The results reveal that as the Sc content increases from 5at% to 20at%, the volume fraction of the Al_3Sc phase in the alloy increases from 26.9% to 80.2%, and the average grain size of the Al_3Sc phase increases from 12.9 μm to 67.7 μm during this period. Additionally, both the coefficient of thermal expansion (CTE) and thermal conductivity (TC) of AlSc alloys exhibit a downward trend. Based on experimental data and first-principles calculations, the effective medium theory and the Turner model effectively predict the TC and CTE of Al-*x*Sc alloys. The optimal characteristic parameter (k_0) of the Turner model is determined to be 50. The model predictions align well with the experimental results.

Key words: AlSc alloys; first principles; microstructure; thermophysical properties

1 Introduction

With the continuous advancement of AlN piezoelectric thin film material preparation technology, FBAR/BAW filters that utilize an aluminum nitride (AlN) piezoelectric resonant element have been widely used in the 4G/5G communication industry. However, AlN itself is a piezoelectric material with relatively poor performance and low coupling efficiency. Studies have shown that doping AlN films with scandium (Sc) can significantly improve their piezoelectric performance. Published research indicates that doping AlN with 43at% Sc can enhance piezoelectric performance (K^2_{eff}) to 27.6 $pC \cdot N^{-1}$, five times higher than that of pure AlN, making such materials highly favored by manufacturers for the fabrication of high-frequency, high-performance, and wide-bandwidth FBAR/BAW devices[1–4]. The AlSc alloy sputter targets used in the preparation of AlScN piezoelectric films represent a core material for 5G radio frequency (RF) filters. Leading international RF filter manufacturers, including Broadcom, Qorvo, and Skyworks, have recognized the potential of AlScN products[5-6].

In industrial production, the most mature method for preparing AlScN thin films is reactive sputtering of an AlSc alloy sputter target in a nitrogen-containing atmosphere. This process enables atomic-level reactions to form high-quality piezoelectric films on substrate materials[7]. For large-sized aluminum scandium alloy targets used in wafer manufacturing, the target assembly is composed of a target that meets the sputtering performance and a backing plate that bonds to the target while maintaining certain strength[8–9]. To achieve stable sputtering under high-power conditions, the AlSc alloy target assembly must exhibit excellent thermal stability, thermal conductivity (TC), and mechanical properties. Thus, the selection of high TC/high-strength

Received date: December 13, 2024
Foundation item: National Key Research and Development Program of China (2022YFB3504402, 2023YFB3610101)
Corresponding author: Yang Hongbo, Ph. D., Professor, GRIREM Advanced Materials Co., Ltd, Beijing 100088, P. R. China, Tel: 0086-10-6159666, E-mail: yanghongbo203@grirem.com

backing materials, as well as the adoption of high-bonding-strength welding method, is crucial[10]. Therefore, it is necessary to systematically investigate the effects of different Sc contents on the microstructure and thermophysical properties of AlSc alloys for the development, optimization, and application of welding processes for AlSc alloy targets.

The thermophysical properties of alloy targets are closely related to their welding processes and applications[11–12]. The thermophysical properties of sputtering targets mainly include parameters such as the coefficient of thermal expansion (CTE), TC, and specific heat capacity. These physical properties directly affect the behavior of the target material during the welding process[13]. For instance, during the diffusion welding process, the large difference in CTE between the target material and the backing plate material causes thermal stress concentration at the welding interface during cooling, leading to deformation of the target material and the generation of micro-crack defects on the welding surface, and ultimately reducing joint strength or causing welding failure[8–9]. Additionally, TC affects heat transfer during welding and sputtering, while specific heat capacity influences the heating rate of materials. The Al-Sc binary phase diagram reveals that the melting point difference between Al and Sc metal is nearly 900 ℃, and the solubility of Sc in Al is very low, challenging alloying during the smelting process. The formation of intermetallic compounds such as Al_3Sc, Al_2Sc, AlSc, and $AlSc_2$, between Al and Sc are hard and brittle, rendering them prone to brittleness and poor heat dissipation in Al-Sc alloys[7]. Hence, there are great difficulties in bonding aluminum scandium alloy targets with high Sc content to metal backing plates.

Currently, the research on AlSc alloys mainly focuses on the effects of Sc additions on the microstructure regulation and mechanical property enhancement of traditional structural alloys like Al alloys and Mg alloys. Moreover, the Sc content in such studies is very low, with a prevailing emphasis on trace or low-dose additions. Bo et al[14] investigated the effects of Sc content on the grain size, phase structure, and phase distribution of AlSc alloys. Yang et al[15] found that 0.3at% Sc doping can improve the thermal stability and high-temperature performance of AlSc alloys, especially the TC and CTE. Sun et al[16] investigated phase transitions in the binary Al-Sc system using first-principles calculation together with cluster expansion, revealing a phase transition from fcc Al to hcp Sc via a bcc intermediate structure as a function of Sc concentration. In recent years, Reshak[17], Chen[18], Pan[19], and Yan[20] et al have conducted research on the structure, elastic modulus, mechanical properties, and intrinsic brittleness of Al-Sc intermetallic compounds, elucidating the intrinsic ductility-brittleness evolution mechanisms in Al_3Sc, Al_2Sc, and AlSc compounds. These studies have significantly enhanced the understanding of the intrinsic plasticity-brittleness behavior in AlSc alloy targets from an electronic structure perspective. However, systematic research on how different Sc contents affect the microstructure and thermophysical properties of AlSc alloys, with a specific focus on the engineering applications of AlSc targets, remains lacking.

First-principles calculations can accurately determine various properties of intermetallic compounds, driving their widespread utilization[21–24]. By combining computational predictions with experimental validation, researchers gain a comprehensive understanding of the impact of intermetallic compounds in different welding processes[24]. This study investigated the effects of Sc content on the microstructure, density, CTE, and TC of Al-*x*Sc alloys (*x*=5, 10, 15, 20, 25, at%). Through first-principles, the structure and thermophysical properties of binary Al-Sc system compounds were obtained. The relationship between microstructure and thermophysical properties of alloy was explored, and the effect of Sc content on the microstructure, CTE, and TC was quantified. In a word, this work provides fundamental data for the development of high-quality AlSc alloy targets.

2 Experiment and Computation

2.1 Experiment

High-purity metals, i. e., 99.999wt% (5N) aluminum (Al) and 99.95wt% (3N5) scandium (Sc), were used as raw materials to prepare Al-*x*Sc alloys (*x*=5, 10, 15, 20, 25, at%) via vacuum induction melting, sequentially labeled as A5S, A10S, A15S, A20S, and A25S, respectively. After heated to 50–150 ℃ above the alloy melting point, the melt was held at this temperature for 10–30 min, then rapidly cooled to room temperature by pouring into a water-cooled copper mold, yielding Al-*x*Sc alloy ingots with different Sc contents. The main components and major impurities of the alloy were analyzed by inductively coupled plasma atomic emission spectroscope (ICP-AES) with a PerkinElmer Optima 8300 instrument, and the results are shown in Table 1.

Table 1 shows that AlSc alloys with a wide range of composition prepared via the melting method exhibit stable main-elements composition, with values closely matching the

Table 1 Chemical composition of Al-*x*Sc alloys (wt%)

Nominal Alloy	Theoretical values		Actual test value							
	Sc	Al	Sc	Si	Fe	Ni	Cu	C	O	Other impurity
A5S	8.06	Bal.	8.02	0.0004	0.0003	0.0002	0.0002	0.0010	0.0033	＜0.005
A10S	15.62	Bal.	15.21	0.0008	0.0010	0.0011	0.0003	0.0014	0.0072	＜0.005
A15S	22.72	Bal.	22.62	0.0019	0.0015	0.0023	0.0005	0.0017	0.0094	＜0.005
A20S	29.41	Bal.	29.07	0.0026	0.0020	0.0028	0.0010	0.0020	0.0145	＜0.005
A25S	35.71	Bal.	35.57	0.0037	0.0029	0.0041	0.0016	0.0024	0.0210	＜0.005

theoretical values. The primary impurities in the alloys are Si, Fe, Ni, Cu, C, and O. As the Sc content increases, the purity of the AlSc alloys gradually decreases, while the oxygen content increases. This can be attributed to two primary factors. First, higher Sc content in the AlSc alloy induces more impurities from the metallic Sc raw material. Second, the increased reactivity of the AlSc alloy with higher Sc content leads to significant contamination from crucible impurities and environmental contaminants, especially gas-phase impurities, during the melting process. Thus, the alloy purity decreases. When the Sc content is less than 15at%, the purity of the AlSc alloy exceeds 99.99wt% , and the oxygen content remains below 100 μg/g. However, when the Sc content reaches 20at% or higher, the purity of the AlSc alloys decreases to 99.95wt%, with oxygen contents ranging from 100 μg/g to 300 μg/g.

The samples was initially polished with sandpaper, followed by fine polishing on a grinding-polishing machine until a mirror-like surface was achieved. Subsequently, the samples were cleaned with deionized water and anhydrous ethanol, and then air-dried using a cold air stream. The microstructural features of the samples, as well as the composition of the intergranular phases, were examined using a Leica DMI3000-M optical microscope (OM) and a JSM-IT700HR scanning electron microscope (SEM). The size of the Al_3Sc particles was measured using Image-Pro image processing software, defined as the average of the two diagonal lengths. To ensure data reliability, over 100 particles were measured from at least three micrographs per sample. Phase composition analysis was performed using a RIGAKU Smartlab 9 kW X-ray diffractometer (XRD) with the following parameters: Cu Kα radiation, operating voltage of 40 kV, operating current of 40 mA, Si standard calibration angle, emission slit DS of 1°, mask of 15, anti-divergence slit AS of 1° , receiving slit RS of 0.2 mm, step size of 0.04° , dwell time of 0.1 s per step, and a scanning angle range of 10°–90°.

Thermal expansion was measured using a DIL402SE dilatometer, and the sample was 6 mm in diameter and 25 mm in length. The measurement was conducted in a nitrogen atmosphere at a heating rate of 5 ℃/min up to 600 ℃. The thermal diffusivity of the Al-*x*Sc alloys was directly measured using the laser flash method (LFA467HT model), and the sample was 9.8 mm in diameter and 2 mm in thickness. Subsequently, the specific heat capacity and density of the samples were determined to calculate TC of the Al-*x*Sc alloys. Once the thermal diffusivity (α), specific heat capacity (C_p), and density (ρ) at temperature T were determined, the TC of the sample was calculated. The C_p was measured using a comparative method; a standard sample with known C_p was placed alongside the Al-*x*Sc alloy samples in the multi-sample laser flash method thermal diffusivity apparatus. The measurement was conducted under identical conditions, and the data were analyzed based on the energy balance equation[25].

$$\lambda = \alpha\rho C_p \quad (1)$$

where λ represents TC ($W\cdot m^{-1}\cdot K^{-1}$), α denotes thermal diffusion coefficient ($cm^2\cdot s$), ρ indicates bulk density ($g\cdot cm^3$), and C_p signifies the specific heat capacity ($J\cdot kg^{-1}\cdot K^{-1}$).

2.2 Computation

In this work, first-principles calculations based on density functional theory were performed using the Vienna *ab initio* Simulation Package (VASP). The electronic exchange-correlation energy was described using the generalized gradient approximation with the Perdew-Burke-Ernzerhof functional[26]. The valence states of Al atoms ($3s^23p^1$) and Sc atoms ($3d^14s^2$) were employed to characterize the electron-ion interactions. For energy convergence, the cutoff energy was set to 500 eV, with energy and force convergence criteria of 10^{-8} and 10^{-5} eV, respectively. The Al_3Sc phase was sampled using a 15×15×15 k-point grid in the irreducible Brillouin zone via the Monkhorst-Pack method. Combined with VASP-phonopy, a 2×2×2 supercell was constructed, and the finite displacement method with the quasi-harmonic approximation was applied to calculate the thermodynamic properties of the optimized Al and Al_3Sc compounds.

3 Results

3.1 Experimental results

3.1.1 Microstructure of Al-*x*Sc Alloys

Fig.1 shows the optical microstructure of Al-*x*Sc alloys. As observed, when the Sc content ranges from 5at% to 20at% , the microstructure of AlSc alloy primarily consists of the α-Al matrix and a secondary phase. The secondary phase is distributed relatively uniformly within the α-Al matrix and primarily presents as large irregular particles, with a few exhibiting 90° angular and square-like morphologies. As the Sc content in the alloy increases, both the quantity and size of the secondary phase increase rapidly. When the Sc content reaches 25at% , the alloys undergo a phase transformation, predominantly becoming single-phase Al_3Sc.

Fig.2 presents XRD patterns of Al-*x*Sc alloys. As shown in the XRD patterns, for Sc contents ranging from 5at% to 20at% , the alloy is primarily composed of α-Al and Al_3Sc phases (the gray particles represent Al_3Sc). With increasing Sc content, the peak intensity of the α-Al phase gradually diminishes, while that of the Al_3Sc phase increases. When the Sc content reaches 25at%, XRD pattern reveals characteristic peaks of the Al_3Sc phase exclusively, which is consistent with OM observations.

Fig.3 and Table 2 show SEM images and EDS results of the primary phases in Al_3Sc and Al-*x*Sc alloys, respectively. As shown in Fig.3, with increasing Sc content, the morphology of the primary bright phase changes. In the A10S alloy, the secondary phase exhibits more angular edges, while the A20S alloy exhibits relatively rounded secondary phase edges, and the particle size significantly increases. The A25S sample predominantly consists of a single phase, which aligns with the metallographic microstructure results. Additionally, SEM image of the A25S alloy reveals numerous small circular holes, which are attributed to casting defects caused by a large solid-liquid shrinkage ratio during the solidification process.

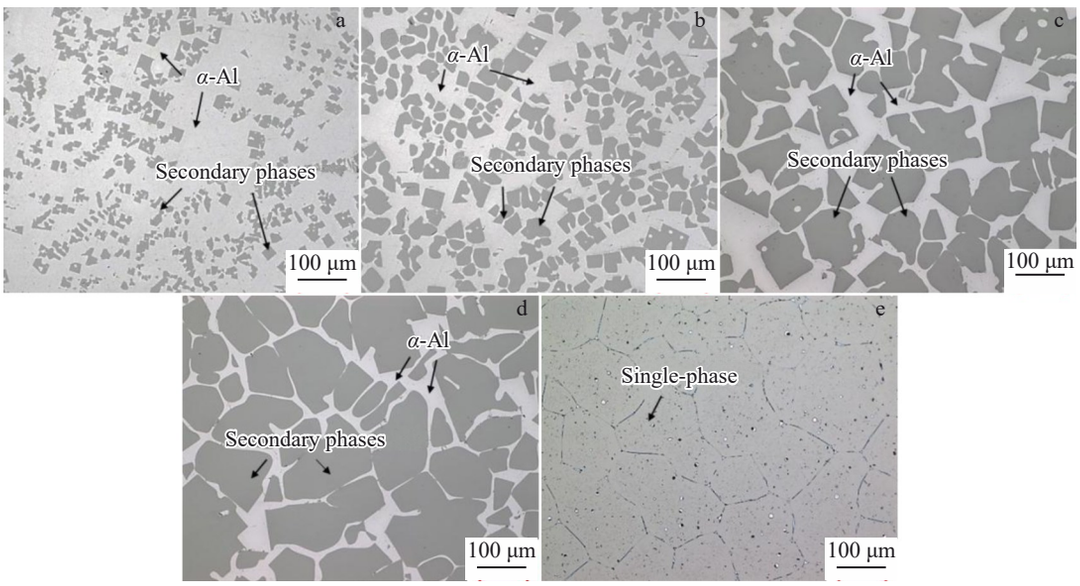

Fig.1 OM images of Al-*x*Sc alloys: (a) Al-5Sc, (b) Al-10Sc, (c) Al-15Sc, (d) Al-20Sc, and (e) Al-25Sc

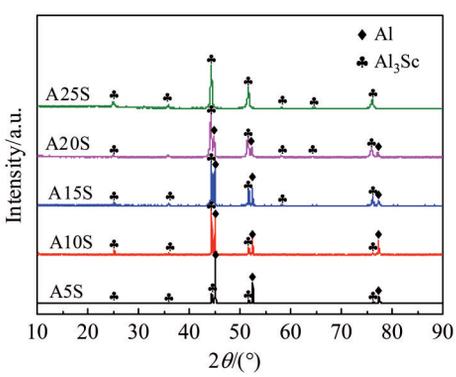

Fig.2 XRD patterns of Al-*x*Sc alloys

EDS analysis of the secondary phase reveals that within the Sc content range of 10at% – 25at% , the concentrations of elements Al and Sc in the secondary phase remain constant. Specifically, the average Sc content is 24.69at% , and the average Al content is 75.31at% , with an Al/Sc atomic ratio of 3.05, which is consistent with the theoretical atomic ratio of Al_3Sc.

Fig. 4 shows the volume fraction and average equivalent circle diameter of the Al_3Sc phase in Al-*x*Sc alloys. As shown, the volume fraction of the Al_3Sc phase in the A5S alloy is 26.9%, with an average equivalent circle diameter of 12.9 μm. In the Al-10Sc alloy, the volume fraction of Al_3Sc phase is 37%, with an average equivalent circle diameter of 24 μm. In the A15S alloy, the volume fraction of the Al_3Sc phase increases to 65.7%, with an average equivalent circle diameter of 59.8 μm. For the Al-20Sc alloy, the volume fraction of Al_3Sc phase is 80.2%, with an average equivalent circle diameter of 67.7 μm. In the Al-25Sc alloy, the volume fraction of Al_3Sc phase is nearly 100%, with an average grain size of 85.4 μm.

3.1.2 Physical properties of Al-*x*Sc alloy

Fig. 5 shows the CTE of Al-*x*Sc alloys at temperatures ranging from 100 ℃ to 500 ℃. The results show that the CTE of AlSc alloys increases gradually with temperature. Furthermore, with increasing Sc content, the variation in the linear CTE with temperature becomes smaller. At 100 ℃, the linear CTEs of A5S and A25S alloys are 22.1×10^{-6} and 12.8×10^{-6} K^{-1}, respectively. At 500 ℃, the linear CTEs of A5S and A25S alloys are 29.9×10^{-6} and 15.6×10^{-6} K^{-1}, respectively. The linear CTE increases by 35% for the A5S alloy and 22% for the A25S alloy, indicating that increasing Sc content reduces the linear CTE of AlSc alloys and diminishes their sensitivity to temperature variations.

Fig. 6 shows the density, specific heat capacity, thermal

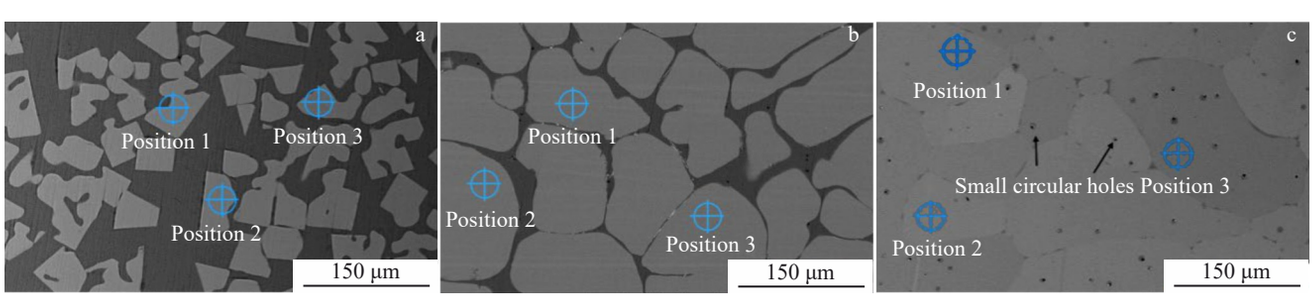

Fig.3 SEM images of Al-*x*Sc alloys: (a) Al-10Sc, (b) Al-20Sc, and (c) Al-25Sc

Table 2 EDS analysis of primary Al_3Sc particles of Al-*x*Sc alloys (at%)

Nominal Alloy	Position 1		Position 2		Position 3		Average	
	Al	Sc	Al	Sc	Al	Sc	Al	Sc
A10S	75.31	24.69	75.51	24.49	75.39	24.61	75.40	24.60
A20S	75.35	24.65	74.77	25.23	75.16	24.84	75.10	24.90
A25S	75.55	24.45	75.48	24.52	75.25	24.75	75.43	24.57

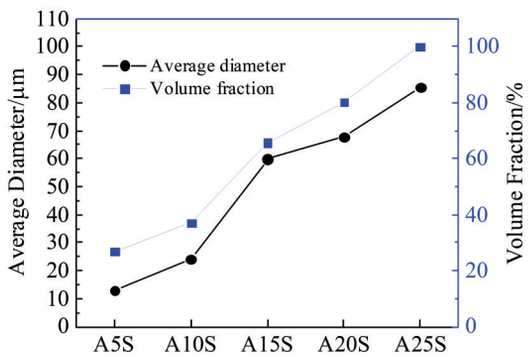

Fig.4 Average diameter and volume fraction of Al_3Sc phase

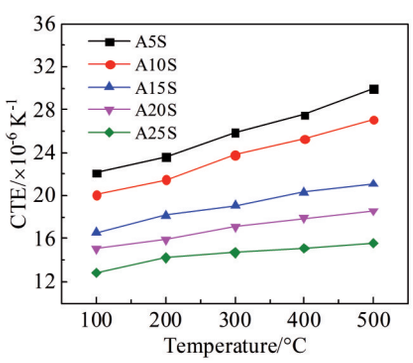

Fig.5 CET curves of Al-*x*Sc alloys at 100–500 °C

diffusivity, and TC of Al-*x*Sc alloys. As shown in Fig. 6a, within the Sc content range of 5at%–25at%, the density of AlSc alloys increases linearly with increasing Sc content. The densities of A5S, A10S, A15S, A20S, and A25S alloys are 2.77, 2.83, 2.86, 2.95 and 2.99 g·cm^{-3}, respectively. A linear fitting of the density of Al-*x*Sc alloys as a function of Sc content gives the equation:

$$\rho_{Al-xSc} = 2.71 + 0.056x \quad (2)$$

where ρ_{Al-xSc} is the density of Al-*x*Sc alloys and x is the atomic percentage of Sc.

Fig. 6b shows that both the specific heat capacity and thermal diffusivity of AlSc alloys gradually decrease with increasing Sc content. Based on the density, specific heat capacity, and thermal diffusivity of the alloys, the TC of AlSc alloys was calculated (Fig.6c). A comparison of TC values for AlSc alloys with different Sc contents reveals that alloys with lower Sc content are more sensitive to temperature changes, with Al-5Sc exhibiting the most significant variation in TC with temperature. The average TC curve of AlSc alloys indicates that as the Sc content increases, the downward trend in TC becomes less pronounced. Between 100 and 500 °C, the average TC of A5S is 197.99 W·m^{-1}·K^{-1}, while A25S has an average TC of only 84.45 W·m^{-1}·K^{-1}, representing a 57.35% reduction in TC.

3.2 The first-principles calculation

3.2.1 Calculation of phase stability of Al-Sc binary system

First-principles calculations were employed to analyze the energy stability of compounds in the Al-Sc binary system, aiming to better explain their correlation with the thermal properties of Al-*x*Sc alloys. The formation enthalpy (ΔH_f) of the bcc, fcc, and hcp ordered structures was calculated as follows:

$$\Delta H_f = (H_{Al_xSc_y} - xH_{Al} - yH_{Sc})/(x+y) \quad (3)$$

where $H_{Al_xSc_y}$, H_{Al}, and H_{Sc} are total energies of ordered Al_xSc_y, fcc Al, and densely-arranged hcp Sc, respectively; x and y are the number of Al and Sc atoms in the Al_xSc_y compound, respectively.

Based on the Al-Sc binary phase diagram and previous research[27–28], the convex hull of the Al-Sc binary system consists of four structures: Al_3Sc with the Ni_3Al-type L_{12} structure (space group: Pm-3m, 221), Al_2Sc with the Cu_2Mg-type C15 structure (space group: Fd-3m, 227), AlSc with the CsCl-type B2 structure (space group: Pm-3m, 221), and $AlSc_2$ with the $InNi_2$-type B82 structure (space group: P63/mmc, 194). To verify the energy differences among compounds under different supercells, formation enthalpies of various intermetallic compounds in the Al-Sc binary system were calculated using 2×2×2, 3×3×3, 4×4×4, and 5×5×5 conventional cells (crystal structures are shown in Fig.7). The results are presented in Fig. 8. A negative formation enthalpy indicates thermodynamic stability of the compound. The black line in Fig. 8 represents the energy convex hull curve for existing compounds. Clearly, Al_3Sc, Al_2Sc, AlSc, and $AlSc_2$ all exhibit negative formation enthalpies at 0 K, with specific values listed in Table 3[13,29]. This demonstrates that Al_3Sc, Al_2Sc, AlSc, and $AlSc_2$ phases in the Al-Sc binary system are thermodynamically stable. The computational results highly align with the literature data, indicating the accuracy of the employed methods.

3.2.2 Thermal properties of Al_3Sc

As shown in Fig. 1 and Fig. 2, when the Sc content is ≤25at%, the Al-Sc binary alloy primarily exists in the form of the stable Al_3Sc phase during the actual solidification process. Therefore, this study focuses on the thermal properties of the Al_3Sc phase. Thermal properties are related to phonons vibrations, so first-principles calculations were performed to compute the phonon energies, from which the thermal

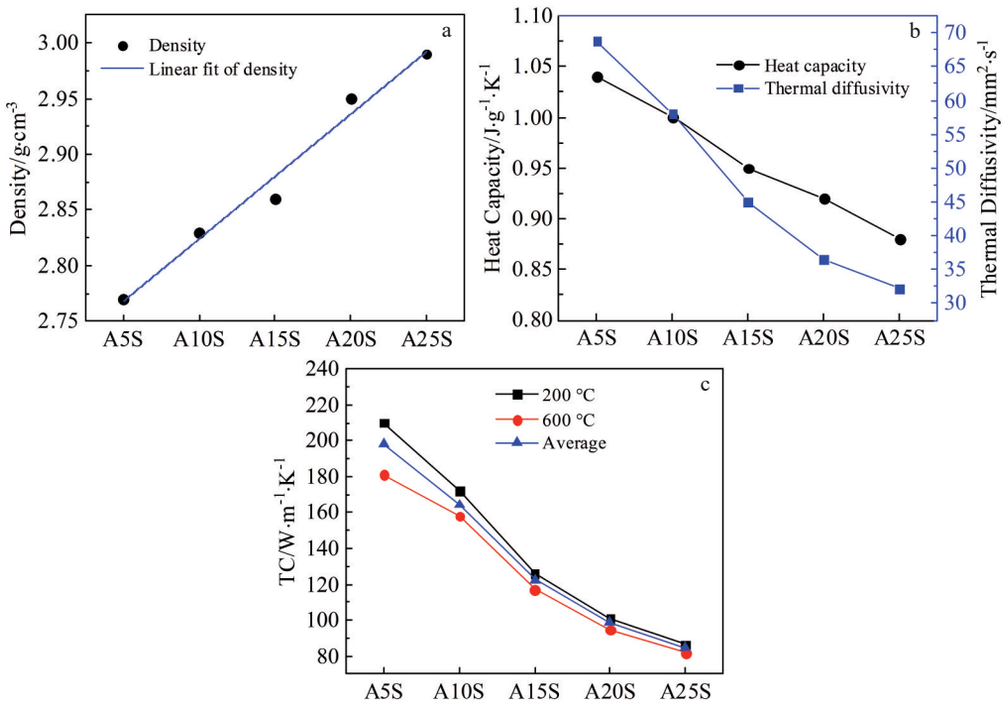

Fig.6 Density (a), heat capacity and thermal diffusivity (b), and TC (c) of Al-*x*Sc alloys

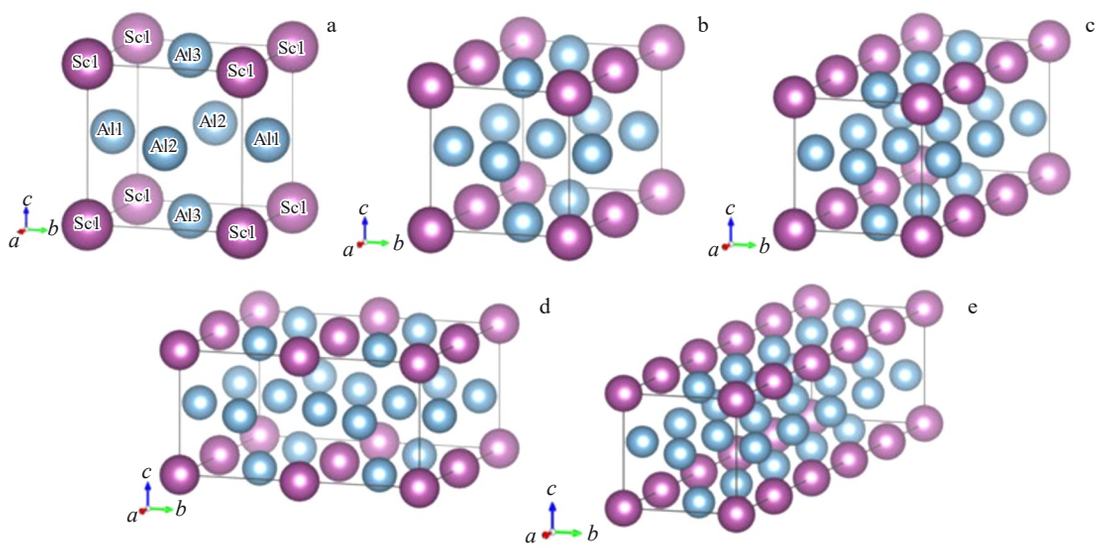

Fig.7 Crystal structures of Al_3Sc with the primitive cell (a), and 2-times (b), 3-times (c), 4-times (d), and 5-times (e) conventional cells

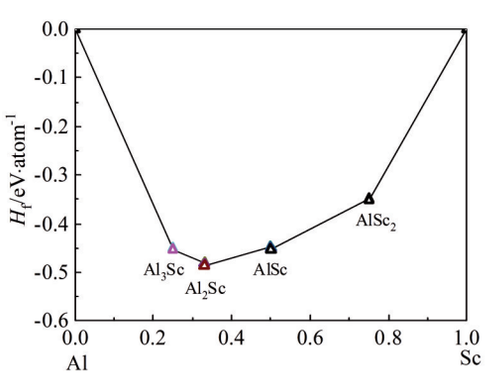

Fig.8 Formation energies (H_f) of Al_3Sc, Al_2Sc, AlSc, and $AlSc_2$ phases

properties of Al_3Sc were derived.

First, the Al_3Sc crystal structure with different volumes was constructed using the finite displacement method. Then, the energy-volume curve was fitted using the Birch-Murnaghan equation of state, and temperature-dependent thermodynamic parameters for the Al_3Sc phase, including bulk modulus, Grüneisen parameter, specific heat capacity, and CTE, were calculated. The calculated CTE values of Al_3Sc are 12.45×10^{-6} K^{-1} at 100 ℃ and 14.95×10^{-6} K^{-1} at 500 ℃.

Fig. 9 shows the total energy distribution of Al_3Sc at different volumes, as well as the free energy distribution curves across different volumes and temperatures (0–1300 K).

Table 3 Formation energies (H_f) of Al_3Sc, Al_2Sc, AlSc, and $AlSc_2$ with the primitive cell and different conventional cells (eV/atom)

Cell	Al_3Sc	Al_2Sc	AlSc	$AlSc_2$
Primitive cell	−0.451	−0.481	−0.448	−0.349
Conventional cell*2	−0.451	−0.481	−0.448	−0.349
Conventional cell*3	−0.451	−0.482	−0.450	−0.350
Conventional cell*4	−0.451	−0.482	−0.453	−0.351
Conventional cell*5	−0.453	−0.485	−0.453	−0.351
Ref.[29]	−0.455	−0.486	−0.455	−0.352
Ref.[13]	−0.452	−0.484	−0.453	−0.335

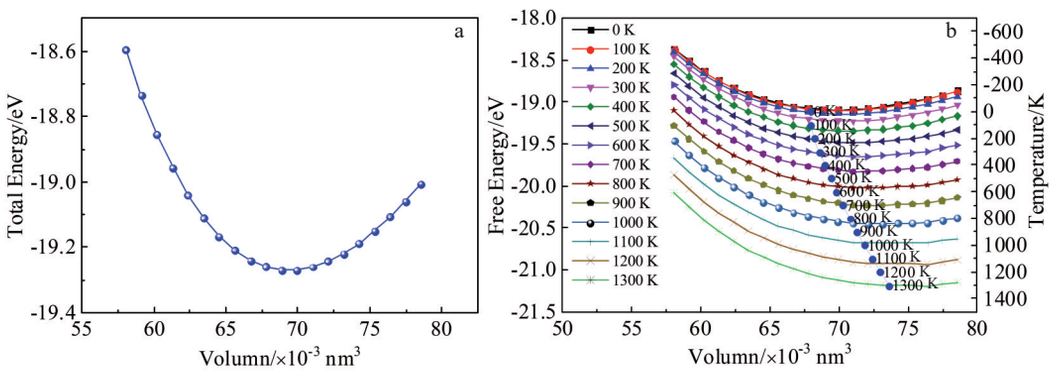

Fig.9 Changes of total energy with cell volume of Al_3Sc at 0 K and 0 GPa (a); change of free energy of Al_3Sc with cell volume and temperatures, as well as the equilibrium volume (blue line) at different temperatures (b)

Fig.9a presents the total energy of Al_3Sc at the corresponding volume. At 0 K and ambient pressure, the most stable volume of Al_3Sc is 68.8×10^{-3} nm³, corresponding to a total energy of −19.3 eV. Fig.9b shows how the free energies of Al_3Sc vary with cell volume and temperature, and illustrates the equilibrium volume of Al_3Sc alloy at different temperatures. From 0 K to 1300 K, as the temperature increases, the equilibrium volume of Al_3Sc alloy increases, and correspondingly, the free energy decreases. The increase in equilibrium volume is primarily due to lattice vibrations and thermal expansion.

Fig. 10 presents the temperature-dependent behavior of

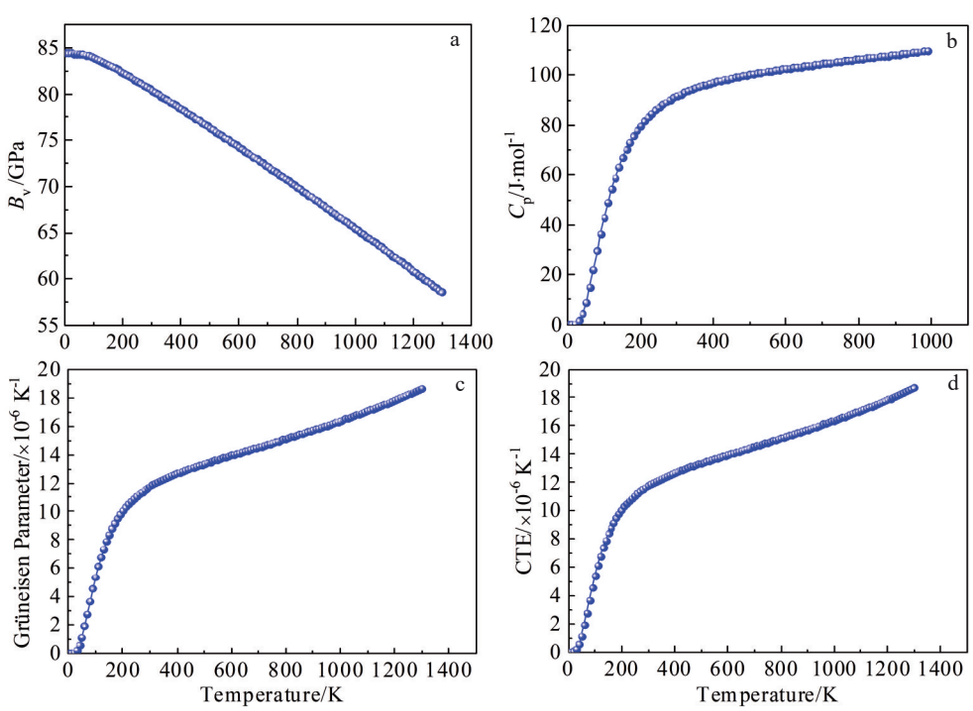

Fig.10 Change of B_v (a), C_p (b), Grüneisen parameter (c), and linear CTE (d) of Al_3Sc with temperature

several thermophysical properties of the Al_3Sc phase, including the bulk elastic modulus (B_v), specific heat capacity (C_p), Grüneisen parameter, and linear CTE. As depicted in Fig. 10a, the bulk modulus exhibits a downward trend with increasing temperature. Conversely, the specific heat capacity of Al_3Sc demonstrates a consistent increase with temperature, as illustrated in Fig. 10b. The variation of the Grüneisen parameter with temperature is shown in Fig. 10c. Notably, the Grüneisen parameter remains positive within the temperature range of 0 K to 1000 K, indicating that Al_3Sc possesses thermal expansion characteristics. Additionally, the linear CTE for Al_3Sc increases sharply at lower temperatures and gradually levels off at higher temperatures. This behavior signifies that the volume of Al_3Sc expands in response to temperature changes, corroborating the findings in Fig.9 and Fig.10c.

3.2.3 Electronic structure

The energy bands and density of state (DOS) of the Al_3Sc compound in both spin-down and spin-up configurations were calculated, and the results are shown in Fig. 11. Fig. 11a displays the energy bands and DOS of the Al_3Sc compound. The energy band structure exhibits identical distributions for spin-up (Al_3Sc-up) and spin-down (Al_3Sc-down) orbitals, which is why the energy bands for the spin-up and spin-down states overlap in Fig.11a.

Fig. 11b presents the total density of state (TDOS) for both spin-up (TDOS-up) and spin-down (TDOS-down) channels, including the energy level splitting of Sc atom orbitals: s orbitals (Sc(s)up, Sc(s)down), p orbitals (Sc(p)up, Sc(p) - down), and d orbitals (Sc(d-t2g)up, Sc(d-t2g)down, Sc(d-eg)up, and Sc(d-eg)down), as well as the corresponding contributions from the Al atom s orbitals (Al(s)up, Al(s)down) and p orbitals (Al(p)up, Al(p)down). It is evident that the DOS distribution for both the spin-up and spin-down channels of the Al_3Sc compound is nearly identical, and the TDOS for the system primarily originates from the contributions of the d orbitals of the Sc atom.

4 Discussion

4.1 Relationship between microstructure and CTE

The CTE of Al-*x*Sc alloys is primarily influenced by the inherent properties, content, and distribution of the precipitated phases. Fig. 12 shows the first-principles calculation results for the thermal expansion behavior and bulk modulus of the α-Al matrix and Al_3Sc phase in the temperature range of 0 – 1000 K. As shown in Fig. 12a, the CTEs of both the α-Al matrix and Al_3Sc phase increase gradually with temperature, but the CTE of the Al_3Sc phase is significantly lower than that of the α-Al matrix.

The bulk modulus of both phases varies inversely with their CTE values. A higher bulk modulus indicates greater resistance to deformation, which results in a lower CTE. As the temperature rises, the vibration amplitude of Al and Sc atoms increases, leading to anharmonic lattice vibrations. However, since the bulk modulus of Al_3Sc is higher than that of the Al matrix, its expansion rate remains smaller. In this case, a large amount of Al_3Sc phase forms and interacts with

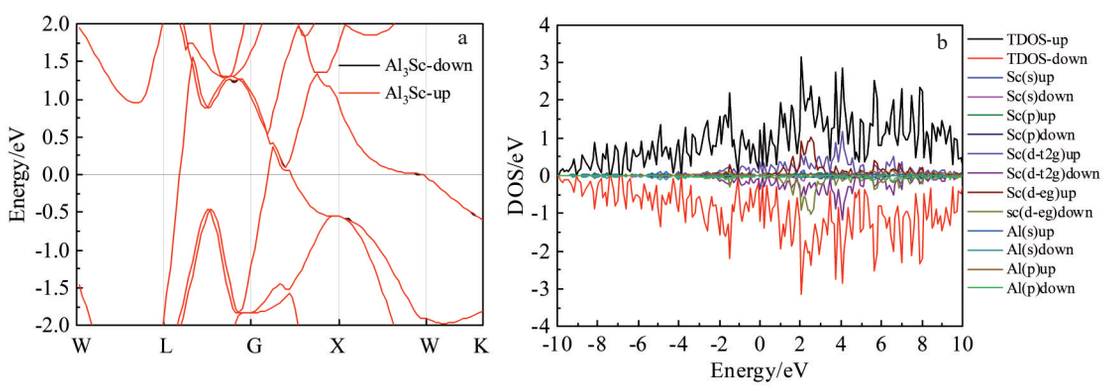

Fig.11 Energy band structures (a) and DOS (b) of Al_3Sc

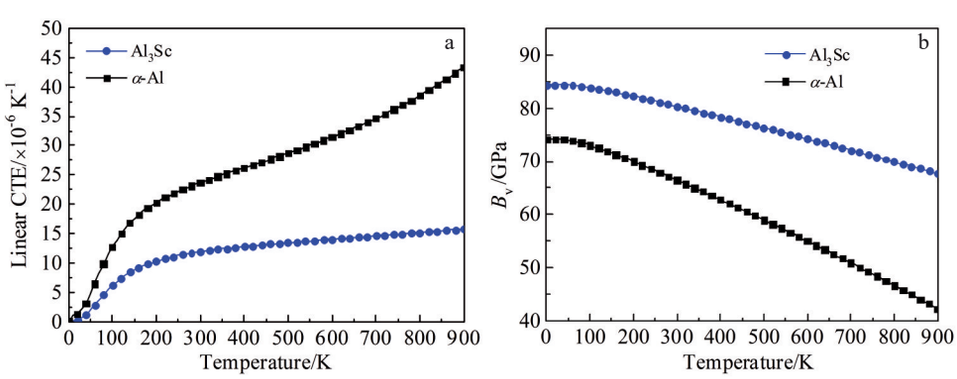

Fig.12 Linear CTE (a) and B_v (b) of α-Al and Al_3Sc at 0–900 K

the Al matrix. The low CTE of Al_3Sc suppresses the thermal expansion of the α-Al matrix, causing a slight reduction in the overall CTE of the alloy.

The high volume fraction of low-CTE Al_3Sc phase can hinder the expansion of the α-Al matrix, leading to a reduction in the slope of the CTE curve. Therefore, as the Sc content increases from 5at% to 25at%, Al atoms are replaced by Sc atoms, and a greater proportion of low-CTE Al_3Sc phase forms. As a result, the volume fraction of Al_3Sc phase significantly increases (Fig. 4), which causes a continuous decrease in the alloy's CTE with the increase in low-expansion Al_3Sc phase.

Researchers have developed various theoretical models to analyze CTE[30–32], considering factors such as phase composition, interphase elasticity, and shear interactions[33]. Previous studies indicate that the Turner model is suitable for describing the relationship between the microstructural evolution of aluminum alloys and their thermal expansion behavior. The Turner model treats the secondary phase as an ideal sphere and accounts for interphase interactions by assuming that each phase undergoes restricted expansion and approximating the internal forces acting on each phase under shear deformation as internal equilibrium stresses[34–35]. The calculation formula is as follows.

$$\alpha_c = \frac{\alpha_p V_p B_p + \alpha_m V_m B_m}{V_p B_p + V_m B_m} \tag{4}$$

where α_p, V_p, and B_p represent the CTE, volume fraction, and bulk modulus of the Al_3Sc phase, respectively; α_m, V_m, and B_m denote the corresponding properties for the Al matrix. The predicted CTE of the Al-xSc alloy is represented by α_c.

The volume fraction V_p of Al_3Sc in AlSc alloys with different Sc contents is shown in Fig.4, by which the volume fraction V_m of α-Al is defined as 100%–V_p. By substituting the bulk modulus and volume fractions of α-Al and Al_3Sc at different temperatures into the Turner model, the predicted CTE of the AlSc alloys is obtained. These predictions are compared with the experimental values, and the results are shown in Fig. 13. CTEs of the alloys increase gradually with the increase in temperature at different Sc contents, and the Turner model calculations are in good agreement with the experimental results. This confirms that the Turner model can accurately predict the CTE of Al-xSc alloys.

4.2 Relationship between microstructure and TC

The TC of alloys is governed by free electron migration and lattice vibration, with electronic conduction being the dominant mechanism[25]. AlSc alloys contain a large number of free electrons, which transfer energy from high- to low-temperature regions through inter-electron collisions. As the Sc content in the alloy increases, numerous irregular, particle-like Al_3Sc phases form randomly in the Al matrix. As shown in Fig. 1 and Fig. 2, these phases hinder free electron movement. At the same time, the volume fraction of Al_3Sc increases significantly. When the Sc content increases from 5at% to 20at%, the volume fraction of Al_3Sc increases from 26.9% to 80.2%. Therefore, when the Sc content reaches

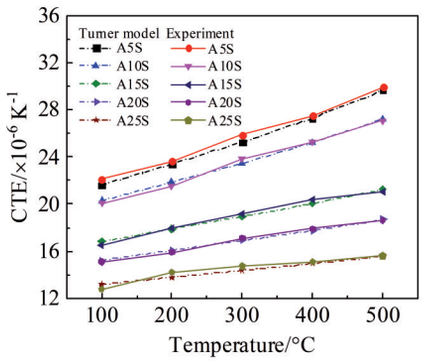

Fig.13 Comparison of CTE values obtained by experiment and Turner model predictions for Al-xSc alloys at different temperatures

20at%, the volume fraction and size of Al_3Sc increase dramatically, resulting in a larger interface between the Al_3Sc phase and the Al matrix. The scattering effect of free electrons increases, reducing the mean free path of free electrons and deteriorating the TC of the alloy.

To further analyze the effect of Sc content on the TC of AlSc alloy, a TC model was used to analyze the relationship between the microstructural evolution and TC. The melting temperature of Al_3Sc reaches 1320 ℃, and the maximum solubility of Sc is only 0.42at% at the eutectic temperature of 660 ℃[36]. This solubility drops significantly at room temperature, meaning that Sc primarily exists in the form of compounds in AlSc alloys. Therefore, Al-xSc alloys can be considered as composites composed of Al_3Sc and α-Al matrix. With the increase in Sc content, the quantity, size, and distribution of the Al_3Sc phase in the alloy evolve. For the TC analysis of composites with randomly distributed secondary-phase particles, researchers have developed the Effective Medium Theory (EMT) and the General Effective Medium Theory (GEMT)[37]. The GEMT model is more suitable for systems with large differences in morphology and distribution of reinforcing phases. It has been successful applied to TC analysis of Al-Ni, Al-Si binary alloys, Mg-RE binary alloys, and Mg-Ce-Al-Mn alloys[38–39].

$$x = \frac{\sum_{i=1}^{m} \lambda_i \varphi_i \frac{dk_0}{(d-1)k_0 + \lambda_i}}{\sum_{i=1}^{m} \varphi_i \frac{dk_0}{(d-1)k_0 + \lambda_i}} \tag{5}$$

where λ_i and φ_i are the effective TC and volume fraction of different phases, respectively, m is the number of phase groups, d reflects the mode of TC, and k_0 is the characteristic parameter of the material system.

According to the previous reports[40–41], the parameters m=2 and d=3, with the effective TC of Al set as 258 $W \cdot m^{-1} \cdot K^{-1}$. Due to the lack of theoretical values for the effective TC of the Al_3Sc phase, this study experimentally measured the TC of Al_3Sc within the temperature range of 50 – 500 ℃, and the average value of 84.45 $W \cdot m^{-1} \cdot K^{-1}$ was taken as its effective TC. The volume fraction of Al_3Sc is shown in Fig.4, and the volume fraction of the Al matrix was calculated by subtraction.

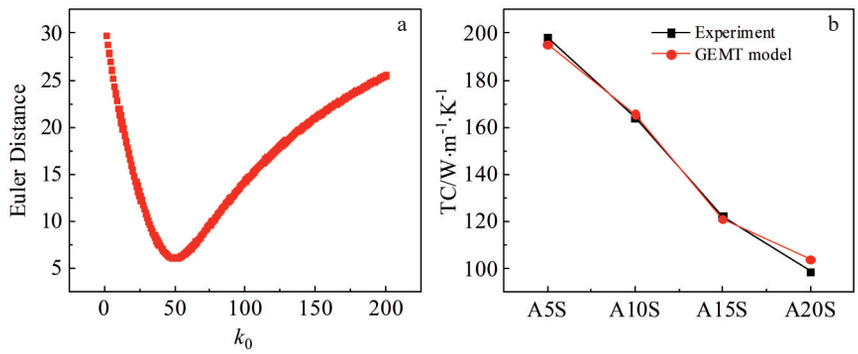

Fig.14 Variation curve of Euler distance predicted by GEMT model with k_0 (a) and comparison of predicted and experimental values of TC (b) of Al-*x*Sc alloy

The value of k_0 was derived from the model fitting by comparing with experimental results, optimized via minimization of the Eulerian distance. The relationship between k_0 and the Euler distance is illustrated in Fig. 14a, where it is evident that the Euler distance is minimized at k_0=50 for the Al-*x*Sc alloy system. Subsequently, the predicted TC of the Al-*x*Sc alloy can be obtained using the GEMT modeling formula. The GEMT model-fitted TC values are displayed in Fig. 14b, which demonstrates a strong correlation with experimental data, thereby validating the model's effectiveness.

5 Conclusions

1) The microstructure of Al-*x*Sc alloys (*x*=5at%–20at%) consists of an α-Al matrix and Al_3Sc phase. As the Sc content increases from 5at% to 20at%, the Al_3Sc phase in the alloy evolves from angular particles to larger, smooth-edged particles, with significant increase in both volume fraction and particle size. When the Sc content reaches 25at%, the as-cast alloy is primarily composed of Al_3Sc phase with an average grain size of 85.4 μm.

2) Within the temperature range of 100–500 °C, both the CTE and TC of AlSc alloys decrease with increasing Sc content. At lower Sc content, the CTE of Al-*x*Sc alloys exhibits more pronounced temperature-dependent variations. Specifically, as the Sc content increases from 5at% to 25at%, the TC of AlSc alloys decreases from 197.99 W·m^{-1}·K^{-1} to 84.45 W·m^{-1}·K^{-1}, representing a 57.35% reduction. Meanwhile, the CTE decreases from 22.1×10^{-6} K^{-1} to 12.8×10^{-6} K^{-1}, indicating improved thermal expansion properties.

3) First-principles calculations reveal that the linear CTE of Al_3Sc initially increases sharply with temperature, followed by a gradual rise. The calculated CTE values of Al_3Sc are 12.45×10^{-6} K^{-1} at 100 °C and 14.95×10^{-6} K^{-1} at 500 °C, aligning well with experimental data. Additionally, the Al_3Sc phase exhibits superior thermal expansion performance compared to pure Al, and the TDOS of Al_3Sc primarily originates from of the d-orbitals contributions of Sc atoms.

4) Within the temperature range of 100–500 °C, the Turner model accurately predicts the CTE of Al-*x*Sc alloys, showing good agreement with experimental results. Furthermore, the GEMT model provides relatively accurate predictions for the TC of Al-*x*Sc alloys.

References

1 Akiyama M, Kano K, Teshigahara A. *Applied Physics Letters*[J], 2009, 95(16): 162107

2 Agnė Ž, Christopher T, Ferenc T *et al. Acta Materialia*[J], 2015, 94: 101

3 Milena M, Johan B, Ilia K *et al. Vacuum*[J], 2011, 86: 23

4 Akiyama M, Umeda K, Honda A *et al. Applied Physics Letters*[J], 2013, 102(2): 021915

5 Zywitzki O, Modes T, Barth S *et al. Surface and Coatings Technology*[J], 2017, 309: 417

6 Men K, Liu H, Wang X Q *et al. Journal of Rare Earths*[J], 2023, 41(3): 434

7 Wang Xingquan, Wang Yu, He Jinjiang *et al. Chinese Journal of Rare Metals*[J], 2023, 47(2): 303 (in Chinese)

8 Wu Daogao, Chen Dehong, Wang Zhiqiang *et al. China Patent*, 202011543862.0[P]. 2020 (in Chinese)

9 Ge Chunqiao, Chen Lu, Li Qiang *et al. Metallic Functional Materials*[J], 2017, 24(6): 23 (in Chinese)

10 Xu Guolin, Luo Junfeng, Wang Xiaoyong *et al. China Patent*, 202010702124.X[P]. 2020 (in Chinese)

11 Yu M R, Zhao H Y, Jiang Z H *et al. Journal of Materials Science & Technology*[J], 2019, 35(8): 1543

12 Chidambaresh S, Radhika N, Deepak N H *et al. Advances in Materials and Processing Technologies*[J], 2023, 10(3): 1

13 Carvalho G H S F L, Galvão I, Mendes R *et al. Defence Technology*[J], 2023, 22: 88

14 Bo H, Liu L B, Jin Z P. *Journal of Alloys and Compounds*[J], 2010, 490(1–2): 318

15 Yang C, Cheng P M, Chen B A *et al. Journal of Materials Science & Technology*[J], 2022; 96: 325

16 Sun M Y, Mao H, Xu D J *et al. Journal of Materials Research and Technology*[J], 2023, 26: 3803

17 Reshak A H, Charifi Z, Baaziz H. *J Solid State Chem*[J], 2010, 183(6): 1290

18 Chen D, Chen Z, Wu Y *et al. Computational Materials Science*[J], 2014, 91: 165

19 Pan R K, Wang H C, Shao L *et al. Comput Mater Sci*[J], 2016, 111: 424

20 Yan K, Chen Z W, Zhao Y N *et al. Journal of Alloys and Compounds*[J], 2021, 861: 158491

21 Wu H Y, Yang G, Li Y *et al. Journal of Materials Research and Technology*[J], 2024, 30: 7485

22 Liu D J, Ma Z, Mao Y J *et al. Materials Today Communications*[J], 2024, 41: 110590

23 Chen J C, Liu Z T, Feng L P *et al*. *Rare Metal Materials and Engineering*[J], 2015, 44(1): 118

24 Wu X J, Fan X L, Wang Sa *et al*. *Rare Metal Materials and Engineering*[J], 2021, 50(2): 483

25 Mo L L, Zhou X, Liu X H *et al. Journal of Materials Research and Technology*[J], 2023, 24: 6227

26 Kresse G, Furthmüller J. *Physical Review B*[J], 1996, 54(16): 11169

27 Wang X Q, Zhao Y, Liu H X *et al*. *Rare Metals*[J], 2024, 43: 3974

28 Gschneidner K A, Calderwood F W. *Bulletin of Alloy Phase Diagrams*[J], 1989, 10(1): 34

29 Stevanović V, Lany S, Zhang X *et al. Physical Review B*[J], 2012, 85(11): 115104

30 Hsieh C L, Tuan W H. *Materials Science and Engineering A*[J], 2007, 460: 453

31 Song M H, Wu G H, Wang N *et al*. *Rare Metal Materials and Engineering*[J], 2009, 38(6): 1043

32 Liu X J, Zhu J H, He Z F *et al*. *Rare Metal Materials and Engineering*[J], 2020, 49(2): 422

33 Daniel R, Holec D, Bartosik M *et al. Acta Materialia*[J], 2011, 59(17): 6631

34 Sharma N K, Misra R K, Sharma S. *International Journal of Solids and Structures*[J], 2016, 102–103: 77

35 Li K, Zhang J, Chen X L *et al. Journal of Materials Research and Technology*[J], 2020, 9(4): 8780

36 Harada Y, Dunand D C. *Materials Science and Engineering A*[J], 2022, 329–331: 686

37 Rocha R P A, Cruz M A E. *Numerical Heat Transfer, Part A: Applications*[J], 2001, 39(2): 179

38 Su C Y, Li D J, Luo A A *et al. Metallurgical and Materials Transactions A*[J], 2019, 50(4): 1970

39 Su C Y, Li D J, Luo A A *et al*. *Journal of Alloys and Compounds*[J], 2018, 747(18): 431

40 Wang J, Carson J K, North M F *et al*. *Int J Heat Mass Tran*[J], 2006, 49: 3075

41 Aksöz S, Ocak Y, Maras Li N *et al*. *Exp Therm Fluid Sci*[J], 2010, 34: 1507

Sc含量对Al-*x*Sc合金微观组织及热物性的影响

吴道高[1,2]，张　璐[1]，徐明磊[1,2]，冯　京[3]，李　栓[1,2]，张小伟[1,2]，王志强[1,2]，杨宏博[1,2]，董瑞锋[1,2]，陈西浩[4]，王　宁[5]

(1. 有研稀土新材料股份有限公司, 北京 100088)

(2. 有研稀土高技术有限公司, 河北 廊坊 065201)

(3. 国标(北京)检验认证有限公司, 北京 100088)

(4. 重庆文理学院 材料科学与工程学院, 重庆 402160)

(5. 西华大学 理学院 高性能科学计算省高校重点实验室, 四川 成都 610039)

摘　要：AlSc合金靶材制备的AlScN压电薄膜是5G射频滤波芯片的核心材料。AlSc合金的热物性及其焊接工艺与应用之间存在密切联系。通过真空熔炼法制备了不同Sc含量的Al-*x*Sc（*x*=5，10，15，20，25，at%）合金，其纯度影响因素主要来源于Sc原材和生产过程。结果表明，随着Sc含量由5at%增加至20at%，合金中Al_3Sc相体积分数由26.9%增加至80.2%，平均尺寸由12.9 μm增加至67.7 μm；AlSc合金的线性热膨胀系数和导热率均呈现下降的趋势。基于实验和第一性原理计算结果，有效介质模型和Turner模型能够分别有效预测Al-*x*Sc合金的导热系数和热膨胀系数，其中Turner模型特征参数k_0最优取值为50，模型预测值与实验值相吻合。

关键词：Al-Sc合金；第一性原理；微观组织；热物性

作者简介：吴道高，男，1986年生，硕士，正高级工程师，有研稀土新材料股份有限公司，北京 100888，电话：010-61590666，E-mail：wudaogao@grirem.com